Photonic Crystal Properties of Self-Assembled Kagome Lattices

A thesis

Presented to the Faculty of the Graduate School

of Cornell University

in Partial Fulfillment of the Requirements of the Degree of

Master of Science

by

Juchen Zhang

May 2020

ABSTRACT

Binary colloidal mixtures are at the frontier for the creation of new photonic crystals (PhCs) because they spontaneously undergo complex ordering at the mesoscale and have the potential to vastly increase the range of structures that can be self-assembled. It is now known that binary mixtures of sub-micrometer shapes form colloidal alloys, i.e., analogous to metalic alloys, determined by the size ratio of the particle populations, the relative concentrations, and the total packing fraction. What is currently unknown is how the multicomponent basis and particle composition in binary colloidal crystals effect photonic dispersion relations. This gap in our understanding of structure-optocal property relationships in colloidal alloys is an important problem because this knowledge will aid in establishing a new paradigm in the colloid-based photonics field and will guide experimentalists to high payoff targets.

Inspired by recent studies showing that binary mixtures of (shape-anisotropic) patchy particles are predicted to self-assemble into a range of Archimedian tilings (ATs), we investigate the photonic properties of the Kagome lattice, i.e., Schläfli symbol $(3 \cdot 6)^2$, using electromagnetic calculations (MIT photonic bands package, MPB) and simulations (MIT Electromagnetic Equation Propagation package, MEEP). The Schläfli symbol represents the cyclic order of triangular- and hexagonal cross-section rods surrounding the vertices, with repeated elements collected as the exponent. We

expected that this strucure would support strong light-matter interactions because it meets the structure factor criteria for large photonic bandgaps, i.e., the static structure factor approaches zero as the wavevector magnitude approaches zero.

In this thesis, we find large bandgaps up to 30% (TM, gap-to-midgap ratio) in the direct $(3 \cdot 6)^2$ structure. The dielectric constants for non-close-packed hexagonal- and triangular rods are varied independently, between 2 and 16, consistent with binary compositions. Mode field distributions indicate that the bandgaps originate from Lorenz-Mie scattering. For inverse structures, bandgaps arise due to dielectric band-air band transitions. Equifrequency contour analysis and finite difference time domain (FDTD) simulations show that negative refraction occurs over all angles of incidence (AANR) for normalized frequencies of 0.27-0.28 ($\varepsilon_{hexagon}$ = 16, $\varepsilon_{triangle}$ = 2), 0.32-0.34 ($\varepsilon_{hexagon}$ = 2, $\varepsilon_{triangle}$ = 16), and 0.32-0.34 (ε_{matrix} = 12). The effective refractive indices reach negative one within these ranges. Sub-wavelength imaging and self-collimation are demonstrated for flatlenses having the $(3 \cdot 6)^2$ structure. These dielectic PhCs provide an alternative to lossy metallic materials for realizing negative refraction in the optical and near-IR region. The photonic properties predicted here are important for applications in waveguides, solid state lighting, nonlinear optics, and superlenses, i.e., imaging beyond the diffraction limit.

BIOGRAPHICAL SKETCH

Juchen Zhang was born and raised in Changchun, China. His interest in the material science & engineering field originated from an advanced chemistry course in high school, which he took to prepare for the national chemistry contest. In 2014 he was admitted to the college of engineering in Peking University and chose material science & engineering as his major. During his time in Peking University, he studied in Dr. Huanping Zhou's group and participated in research on perovskite solar cells. He worked on several projects, which included improving the efficiency of the devices as well as exploring the hysteresis behavior in the solar cells. In addition, he attended the University of Pittsburgh as an exchange student in 2017. In 2018 he was admitted to the Material Science & Engineering department at Cornell University as a Master of Science student. He studied and worked under the supervision of Prof. Chekesha M. Liddell Watson. His work mainly focused on photonic crystals, especially on the refraction properties for Archimedean tiling structures.

ACKNOWLEDGEMENT

There are many people I would like to thank. First, I want to thank my advisor Prof. Chekesha M. Liddell Watson, who gave me support and guidance on my research projects. I will miss our discussions. I would also like to thank Prof. Jin Suntivich who agreed to be a member of my committee and gave me advice regarding my thesis defense and the written thesis. To all the past members of Prof. Watson's group, thank you for your useful data and patient answers, especially Dr. Angela Stelson. To Dr. Huanping Zhou, my advisor in Peking University as well as all the members of Dr. Huanping Zhou's lab, thank you for leading me on the road to a research career. To all my friends who I have made over these years, thank you for your patient listening and all the joy you gave me. Finally, I would like to thank my parents, who showed me great support all of my life, and I would not accomplish anything without them.

TABLE OF CONTENTS

CHAPTER 1

PHOTONIC CRYSTAL PROPERTIES OF SELF-ASSEMBLED KAGOME LATTICES

Introduction

PhCs dramatically alter the dispersion relations and the spatial power distribution of electromagnetic (EM) modes in dielectric materials with a periodic refractive index. Specific designs of PhCs promote photonic bandgaps, i.e., frequency ranges over which propagation is disallowed in the material for all directions and polarizations of light. Tailoring the dispersion relations in PhCs enables a myriad of properties, i.e., spontaneous emission suppression, light-localization, slow light, superlenses, superprisms, sensing, etc.[1-4, 5] These properties have been applied in solid-state lighting and solar cells, waveguides, optical transistors, imaging, beam steering, and anti-counterfeiting security features, respectively, to name a few.[1, 6-9] PhCs are uniquely applicable in these areas because they support remarkably high efficiency and low loss, high resolution beyond the diffraction limit, low detection limits and high selectivity, etc. Thousands of papers are published each year on the fundamental science and engineering applications of PhCs. A variety of parameters including crystal structure, symmetry, dielectric connectivity, dielectric contrast (i.e., ratio of high and

low dielectric constants), and filling fraction (i.e., packing fraction) determine the optical properties of a PhCs.[6, 7]

Recently, new concepts have emerged for predicting structures that may support large photonic bandgaps, namely the arrangements should have a structure factor $S(\boldsymbol{k})$ tending toward zero as $|\boldsymbol{k}|$ approaches zero. Structures that meet the criteria include disordered hyperuniform,[10] continuous random networks,[11] quasicrystals,[12] and Archimedean Tillings (ATs).[13-15] Moreover, these structures may support isotropic photonic bandgaps, unlike the common PhCs. Bandgap isotropy with respect to propagation direction arises from higher order local symmetry of the lattice and is desirable for free-form waveguides (i.e., line defects of arbitrary curvature),[16] flexible cavity design,[17] and out-coupling across all incident angles from light emitting diodes.[18] As illustrated by these studies, periodicity is sufficient, but not necessary for the formation of photonic band gaps.

In the computational study of PhCs, the central goal is predicting the optical properties of photonic materials by modelling dispersion relations, field distributions, and the spatio-temporal evolution of electromagnetic fields. In general, the modeling programs use PhC structures defined by dielectric constants, basis shapes, and crystal lattice to solve Maxwell's equations for light propagation in the material.[19] Combining Maxwell's equations in the frequency domain with Bloch's theorem yields an eigenvalue problem,[20]

$$\nabla \times \left(\frac{1}{\varepsilon(\boldsymbol{r})} \nabla \times \boldsymbol{H}(\boldsymbol{r}) \right) = \left(\frac{\omega}{c} \right)^2 \boldsymbol{H}(\boldsymbol{r}).$$

This master wave equation assumes the material is free of sources (i.e., charges and currents), linear (i.e., dielectric polarization is proportional to the electric field), isotropic (i.e., material permittivity and permeability are scalar), time-harmonic (electric and magnetic fields vary periodically with time), without explicit frequency dependence, and with permeability equal to one. The plane wave expansion method as implemented by MIT Photonic Bands Package, is used to calculate the eigenvalues of the master wave equation for nonhomogeneous materials. The eigenvalues $\omega(\boldsymbol{k})$ correspond to the bands, or modes, in the photonic band diagram (Figure 1). The photonic bandgap is a range of frequencies for which there are no available modes. In the band diagrams, the frequency is normalized by the spatial period, because Maxwell's laws are scale invariant. The bandgap size can be tuned by using a rational choice of structural and materials parameters.

Complementary techniques for modeling the electromagnetic properties of materials include finite difference time domain FDTD simulations. For these numerical simulations, electromagnetic fields are evolved in time using discrete time steps. Because these simulations are performed in the time domain, they are ideal for studying the propagation properties of light in materials, i.e., refraction,[5, 21] lensing,[9] self-collimation,[22] slow light,[23, 24] etc.

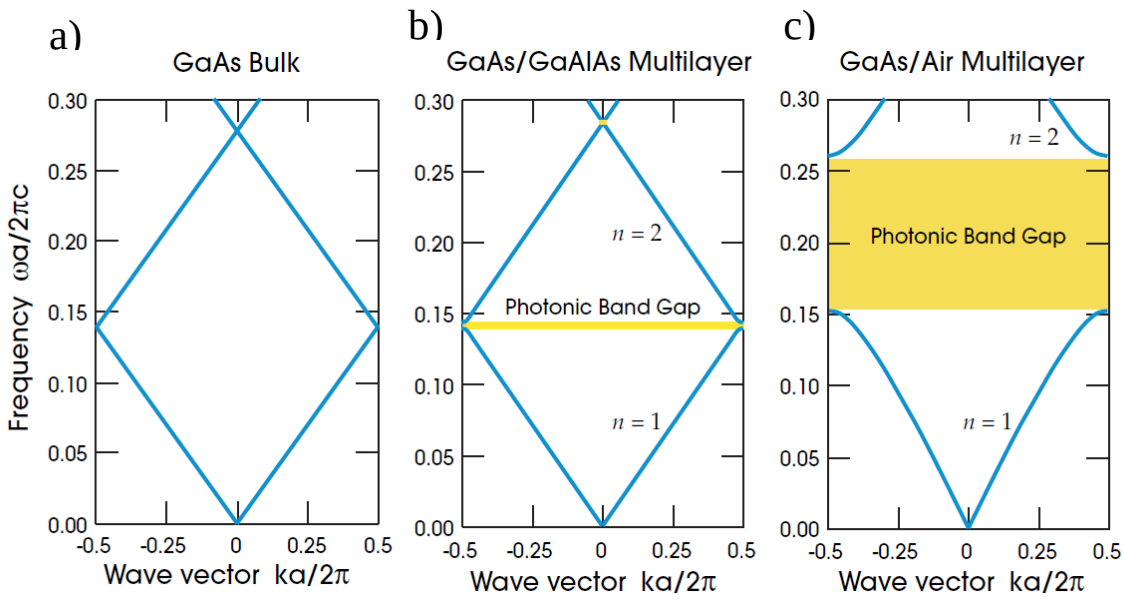

Figure 1. 1-D photonic crystals with periodic dielectric constant values of (a) 13 and 13, (b) 13 and 12, and (c) 13 and 1. The photonic bandgap size increases with dielectric contrast, $\varepsilon_{high}/\varepsilon_{low}$.[20]

However, few studies have addressed these properties that depend on the curvature of the photonic bands themselves rather than on the bandgap, especially in the colloid based photonics field.

Challenges in the Fabrication: Photonic Crystals to Photonic Alloys

Lithographic methods for generating structures have been extensively developed, enabling the fabrication of PhCs with two-dimensional periodicity. Unfortunately, the extension of lithographic engineering into three-dimensional structures using holographic (i.e., interference lithography) techniques is limited by the complexity in optical setups required to produce the necessary interference patterns.[25] Additionally, lithographic processes have manufacturing limitations of feature size and sample area, equipment cost, and clean room environments.[26] Self-assembled colloidal systems offer an attractive alternative to lithographic methods because of their cost-effectiveness, large sample area and the ease of building-up structures in three-dimensions that are active in the visible and near-IR regions.[27]

The self-organization of single-component hard spheres leads to structures with high packing density such as face-centered cubic (FCC), but this structure has no photonic bandgap regardless of refractive index contrast. The inverse FCC packing (inverse opal) has a narrow photonic band gap, between the eighth and ninth photonic bands, which opens due to the isotropy of the Brillouin zone. However, the gap is unstable against minor size polydispersity and positional disorder.[28-31] Symmetry-

induced degeneracy in low-lying bands is lifted for the champion diamond structure, because of its complex basis.[32, 33] The result is a large, stable bandgap between the second and third bands (Figure 2). Because of its low packing fraction, this colloidal structure has only been fabricated through nanorobotic manipulation and DNA-mediated interactions.[34, 35] The drawbacks of these approaches include the laborious and time consuming process and the inconsistent reproducibility[36], respectively.

Shape-binary colloidal crystals are promising for the fabrication of new PhCs because they have the potential to vastly increase the range of structures with strong light-matter interactions that can be self-assembled from simple building blocks. These arrangements also align with the symmetry-reduction strategy (i.e., at the lattice point) that, for example, opens photonic bandgaps in the diamond structure. In recent years, organic and inorganic chemical synthesis routes have been employed to prepare shape-anisotropic colloids in quantities sufficient for self-assembly studies. These synthetic methods include gel-sol precipitation under hydrothermal aging,[37, 38] seeded emulsion polymerization,[39-41] and co-solvent precipitation of fullerenes in good-poor solvent combinations.[42-44] In addition, platelets and rods with polygon cross-sections have been microfabricated by photolithography,[45] stop-flow lithography[46] and PRINT (i.e., Particle Replication In Nonwetting Templates)[47].

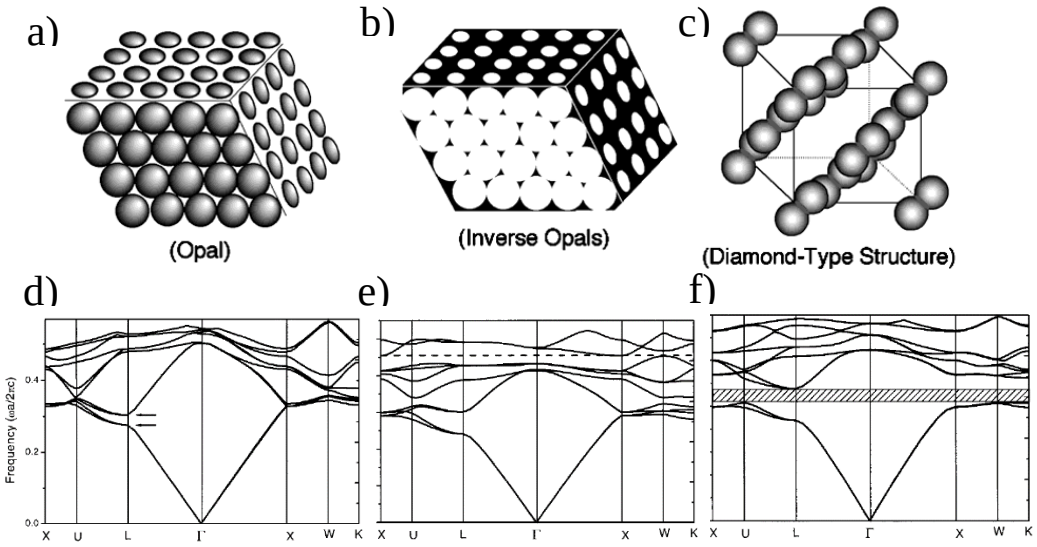

Figure 2. The rationale for reducing the symmetry at lattice points by utilizing anisotropic particle shape and/or complex basis. (a, d) FCC structure and corresponding band diagram, (b, e) Inverse FCC structure and corresponding band diagram, (c, f) Diamond structure and corresponding band diagram. A large, stable band gap is found for the diamond-like structure because the dimer particles overcome symmetry induced degeneracy of the photonic bands at high symmetry points.[32]

Though a diverse palette of monodisperse anisotropic particles has been developed, the experimental assembly of shape-binary colloidal mixtures is still a nascent area and studies of their photonic properties remain scarce.

Binary mixtures of anisotropic particles have been predicted to form ATs in Monte Carlo simulations of hexagonal and triangular platelets with enthalpic shape-specific patches, i.e., interaction between dissimilar shapes favored.[48] However, reports on the photonic properties of such tilings focus on arrangements of high dielectric posts at the vertices of polygons in air, consistent with lithographic fabrication processes. For example, the $3^2 \cdot 4 \cdot 3 \cdot 4$ structure with high dielectric posts at the vertices has nearly 12-fold local rotational symmetry and bandgap variation of 1%–3% over all incident angles, i.e., isotropic bandgap. The structure was found to show left-handedness (i.e., product of group and phase velocity less than zero) and negative refraction for both linear polarizations.[5]

Inspired by recent studies showing that binary mixtures of shape-anisotropic particles may self-assemble into a range of Archimedian tilings, we investigate the photonic properties of tilings based on hexagonal- and triangular cross-section rods, i.e., Kagome lattices, $(3 \cdot 6)^2$. The computational studies herein utilize electromagnetic calculations to determine the effects of the multicomponent basis, particle composition, and particle spacing on photonic bandgap formation. The origin of the bandgaps in the $(3 \cdot 6)^2$ structure is established from the spatial distribution of the electric field density.

The refraction properties of the $(3 \cdot 6)^2$ structure are clarified by analyzing contours of equal frequency (EFCs). FDTD simulations are used to visualize the anomolous refraction and imaging properties. Overall, enhancing our understanding of the structure-optical property relationships in shape-binary PhCs is important to catalyze their development as a new topological class for colloid-based photonic applications.

Computational Methods

The structural model of the $(3 \cdot 6)^2$ AT is composed of one hexagon- and two triangle cross-section rods on a hexagonal lattice, consistent with p6mm plane group symmetry [Figure 3(a)]. The unit lattice vectors are given by $\boldsymbol{a_1} = (\sqrt{3}/2,\ 1/2,\ 0)$ and $\boldsymbol{a_2} = (\sqrt{3}/2,\ -1/2,\ 0)$. The side lengths of the rods L are described by the basis size parameter R, where $L = R|\boldsymbol{a}|/2$ for tangent rods. The basis size parameter is the fractional side length with respect to the tangent rod case (i.e., R = 1), and was varied from 0.7 to 0.9. The location of the hexagonal rods is chosen to be the origin of the unit cell, and accordingly, the triangle rods are centered at the points ($a/3,\ a/3,\ 0$) and ($2a/3,\ 2a/3,\ 0$), where the lattice constant magnitude a = 1. The dielectric filling fraction η_d describes the area fractions of the rods and matrix weighted by their respective dielectric contrasts with air. The filling fraction parameter as a function of R was calculated from the expression,

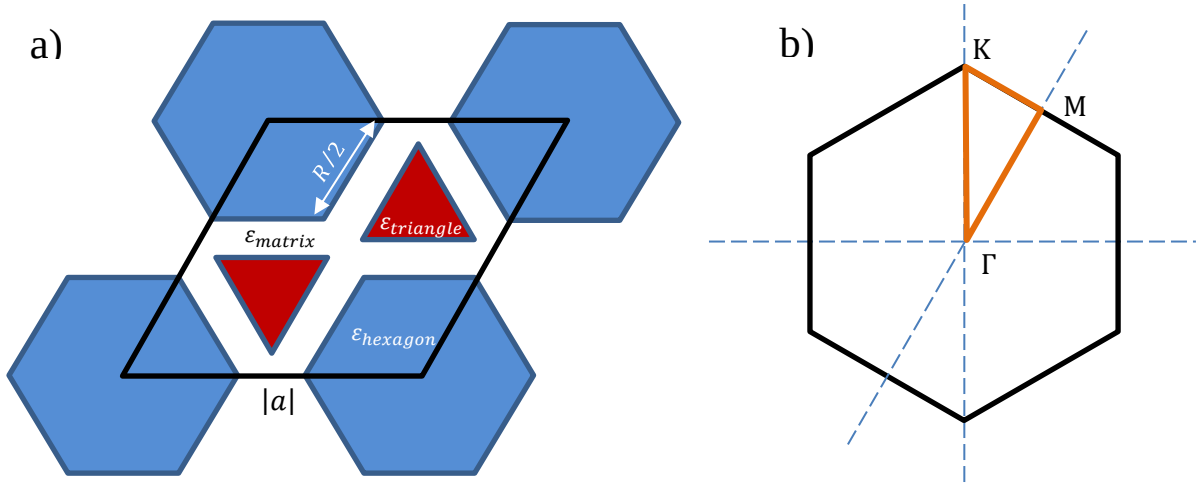

Figure 3. (a) Schematic of the $(3 \cdot 6)^2$ tiling composed of dielectric hexagonal and triangular rods. (b) Hexagonal Brillouin zone of this structure, with the irreducible Brillouin zone and high symmetry points highlighted.

$$\eta_d = 0.75\varepsilon_{hexgaon}R^2 + 0.25\varepsilon_{triangle}R^2 + \varepsilon_{matrix}(1 - R^2)$$

The photonic band structure was calculated using the MIT Photonic Bands (MPB) software package. Dispersion curves of light frequency versus wavevector were calculated along a path through the high symmetry points of the irreducible Brillouin zone [Figure 3(b)]. The first twenty photonic bands were determined, within a convergence criteria of $\pm 10^{-5}$ %, by interpolating 100 k-points between the points of high symmetry. This high number of k-points provides the detailed band behavior needed to produce equifrequency contours (EFCs). The transverse magnetic (TM) and transverse electric (TE) modes were evaluated for direct and inverse structures (i.e., $\varepsilon_{hexagon} = 1,\ \varepsilon_{triangle} = 1,\ \varepsilon_{matrix} > 1$), and with the dielectric constants ranging from 2 (SiO_2) to 16 (Ge). The resolution grid size of $|a|/32$ yielded a minimum of 4, 096 plane waves. The mesh grid size of 5 was set for averaging the dielectric constant between grid points.

The analysis of the equifrequency contours (EFCs) was conducted in order to establish the refraction properties of the $(3 \cdot 6)^2$ AT. Frequency values were plotted over reciprocal space and interpolated to produce the EFCs. Concave contours with inwardly increasing gradient around a high symmetry k-point indicate negative refraction for a range of incident angles. The wavevector magnitude of the beam incident on a photonic crystal is defined as $|\boldsymbol{k_{incident}}| = \omega|\boldsymbol{a}|/2\pi c$. The component of

the wavevector in the crystal parallel to the surface of incidence is conserved in refraction. Moreover, conservation of energy dictates that the frequency in air and in the photonic crystal are equal, enabling the solutions to be evaluated by a simple geometric analysis. In brief, a construction line (dashed line) perpendicular to $\boldsymbol{k_{parallel}}$ is overlaid on the EFC. The intersections of this line with the PC contours, having frequency equivalent to the incident k-vector, signify the modes that propagate in the PC. In addition, to prevent higher-order Bragg diffraction, an additional constraint is applied to the incident beam frequency, i.e., $\omega|\boldsymbol{a}|/2\pi c \leq 0.5$ (ΓK surface).[48]

The refraction and handedness of the propagating modes are determined by the group velocity $\boldsymbol{v_g} = \boldsymbol{\nabla_k}\omega$ and the phase velocity $\boldsymbol{v_\phi} = \omega/\boldsymbol{k}$. Refraction is distinguished from reflection based on the angle between the perpendicular components of group velocity in air $\left(\boldsymbol{v^{\perp}_{g,incident}}\right)$ and in the PC $\left(\boldsymbol{v^{\perp}_{g,PC}}\right)$, i.e., $\boldsymbol{v^{\perp}_{g,incident}} \cdot \boldsymbol{v^{\perp}_{g,PC}} > 0$ and $\boldsymbol{v^{\perp}_{g,incident}} \cdot \boldsymbol{v^{\perp}_{g,PC}} < 0$, respectively. For negative refraction, both the incident and refracted beams lie on the same side of the surface normal. In other words, the angle between the parallel components of the group velocity in air $\left(\boldsymbol{v^{\parallel}_{g,incident}}\right)$ and in the PC $\left(\boldsymbol{v^{\parallel}_{g,PC}}\right)$ is acute, i.e., $\boldsymbol{v^{\parallel}_{g,incident}} \cdot \boldsymbol{v^{\parallel}_{g,PC}} < 0$. Right-handed and left-handed refraction are defined by the conditions on the group velocity $\left(\boldsymbol{v_{g,PC}}\right)$ and phase velocity $\left(\boldsymbol{v_{\phi,PC}}\right)$ in the PC, i.e., $\boldsymbol{v_{g,PC}} \cdot \boldsymbol{v_{\phi,PC}} > 0$ and $\boldsymbol{v_{g,PC}} \cdot \boldsymbol{v_{\phi,PC}} < 0$, respectively. With higher order diffracted beams eliminated, Snell's law can be applied to calculate the effective index of refraction, n_{eff}.

To further confirm the predictions with respect to refraction properties, we simulated light propagation using MIT Electromagnetic Equation Propagation (MEEP) software package, i.e., finite-difference time-domain method (FDTD). Simulations were performed on the E_z component of the TM polarized source. To simulate the propagation of a beam through a PC, we modeled a Gaussian beam incident on a PC (ΓK surface) with a thickness of 12 unit cells. A perfectly matched layer of thickness $2|\boldsymbol{a}|$ surrounded the simulation region. The Gaussian beam was centered at the edge of the perfectly matched layer in a simulation box of 60 × 40 unit cells. The width of the beam was set to 4 unit cells and the beam propagated for a total of 300 time steps. The time step resolution was $\Delta t = S\Delta x$, where S is the Courant factor and Δx is the spatial resolution of 40. The rods at the PC surface were not truncated at the edge of the unit cell. In addition, superlens properties were investigated via FDTD simulation. Continuous point sources were centered one unit cell away from PCs within a simulation box of size of 20 × 40 unit cells. The simulations were run for a total of 200 time steps for PCs with thickness from 2 to 10 unit cells.

Results and Discussion

The contour maps of the TM bandgap size as a function of basis size parameter R and dielectric contrasts ($\varepsilon_{hexagon}/\varepsilon_{air}$, $\varepsilon_{triangle}/\varepsilon_{air}$) are provided in Figure 4. The direct $(3 \cdot 6)^2$ structure promotes large TM bandgaps, up to 30.0% gap-to-midgap ratio,

over a wide range of structural and materials parameters. Bandgaps between the first and second (1-2), third and fourth (3-4), and sixth and seventh (6-7) bands are simultaneously maximized ($\varepsilon_{hexagon}$ = 16, $\varepsilon_{triangle}$ = 2, R = 0.7). In contrast, the 2-3 bandgap size reaches a maximum for the opposite extreme in composition, $\varepsilon_{hexagon}$ = 2, $\varepsilon_{triangle}$ = 16, R = 0.7. These findings follow the general principle of gap competition for structures having multiple bandgaps,[49] i.e., conditions for large gap sizes are in complementary ranges of structural parameters. The inverse $(3 \cdot 6)^2$ structure (i.e., air rods in high dielectric matrix) exhibits modest TM bandgaps even at high dielectric contrasts, because gaps for this polarization are favored when the displacement field distribution is localized in the dielectric rods, i.e. low connectivity arrangements.[20] The contour map of the TM bandgap size for the 2-3 gap (direct structure) is provided in the Supplementary Information (Figure S1). The plot of gap size as a function of ε_{matrix} for the 3-4 gap (inverse structure) is provided in the Supplementary Information (Figure S2). The TM bandgaps open at low dielectric contrasts, enabling a wider range of materials to be incorporated into the photonic solids such as common polymers (i.e., polystyrene, polymethyl methacrylate) and ceramics (i.e., Al_2O_3, SiO_2). Similar to many photonic structures, large bandgap sizes are found for the $(3 \cdot 6)^2$ structure when its composition can be described by a high dielectric component (i.e., $\varepsilon_{hexagon}$ or $\varepsilon_{triangle}$) in contrast with low dielectric component(s) (i.e., ε_{matrix} and complementary shape).

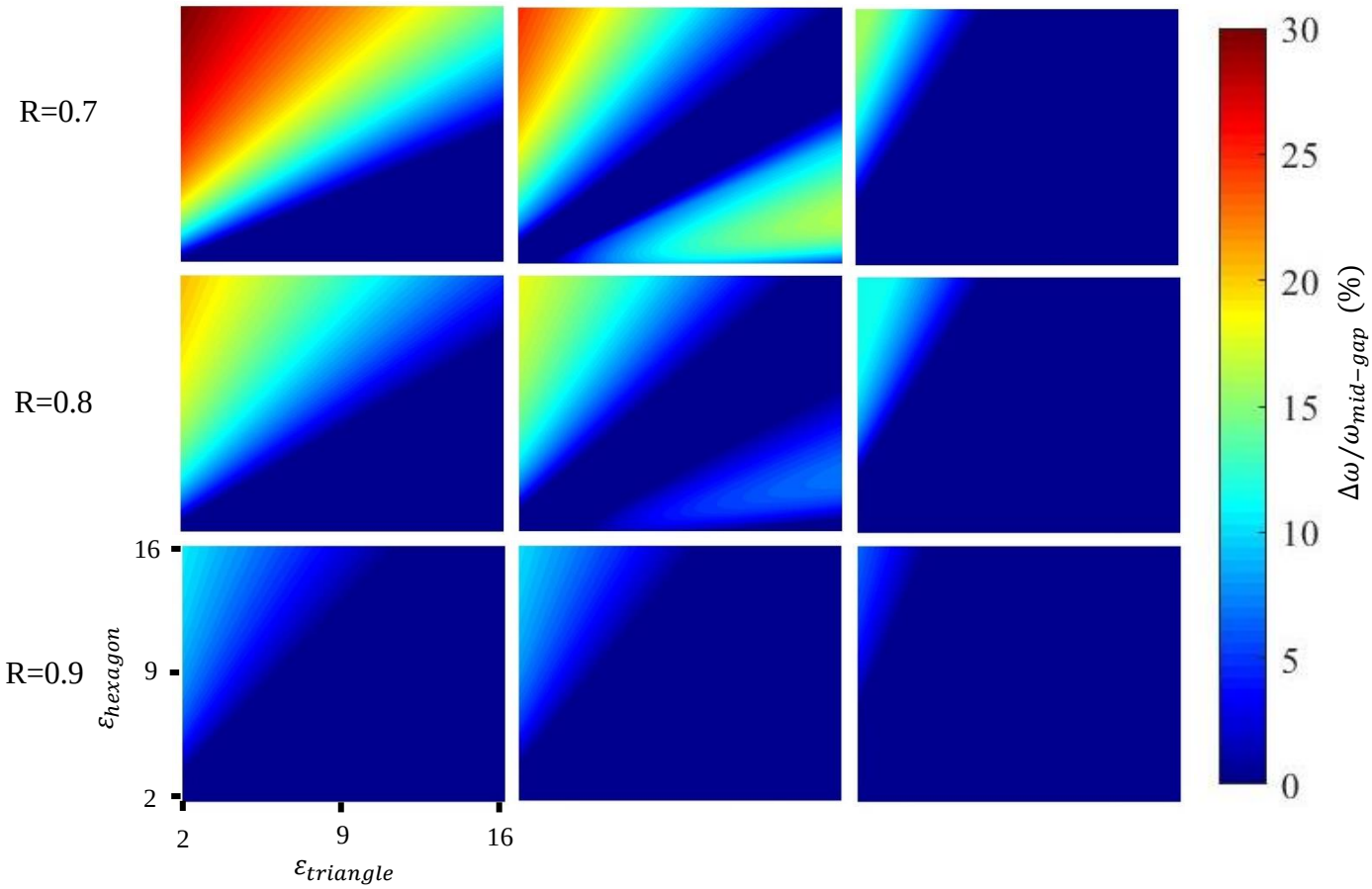

Figure 4. Contour maps of gap size (gap-to-midgap ratio) as a function of dielectric contrasts and basis spacing parameter for the TM polarization in the direct $(3 \cdot 6)^2$ structure.

The TM band diagrams for the direct and inverse $(3 \cdot 6)^2$ ATs are presented in Figure 5. Many bandgaps with gap height above 10% gap-to-midgap ratio are apparent in the dispersion curves for the direct structures. Structures with multiple bandgaps are of interest for systems that require synchronous manipulation of distinct signals, and for photonic isolation of a waveguide light source from electrical contact.[50, 51] In addition, the low frequency bandgaps are defined by largely anisotropic bands, similar to single component PhCs. This result stems from the crystallinity (and 6-fold rotational symmetry) in the $(3 \cdot 6)^2$ structure. These anisotropic bands at the gap edge have been used for negative refraction. Some ATs have higher local symmetry than their Bravais lattices and accordingly show extensive isotropy of bandgaps.[5] The 6-7 bandgap is bounded by isotropic bands, i.e., 3% and 10% change in frequency across the irreducible Brillouin Zone for bands 6 and 7, respectively. Such 'flat' bands in PhCs have been used for slow light properties.[52]

To clarify the mechanism of TM bandgap formation, we examined the electric displacement field (i.e., dielectric constant multiplied by the electric field) distributions for the bands limiting the bandgaps at the Γ high symmetry point. Figures 6 shows the displacement fields for bands 1-8 in the $(3 \cdot 6)^2$ AT with high dielectric hexagonal rods (R = 0.8) [Figures 6(a)-(h)].

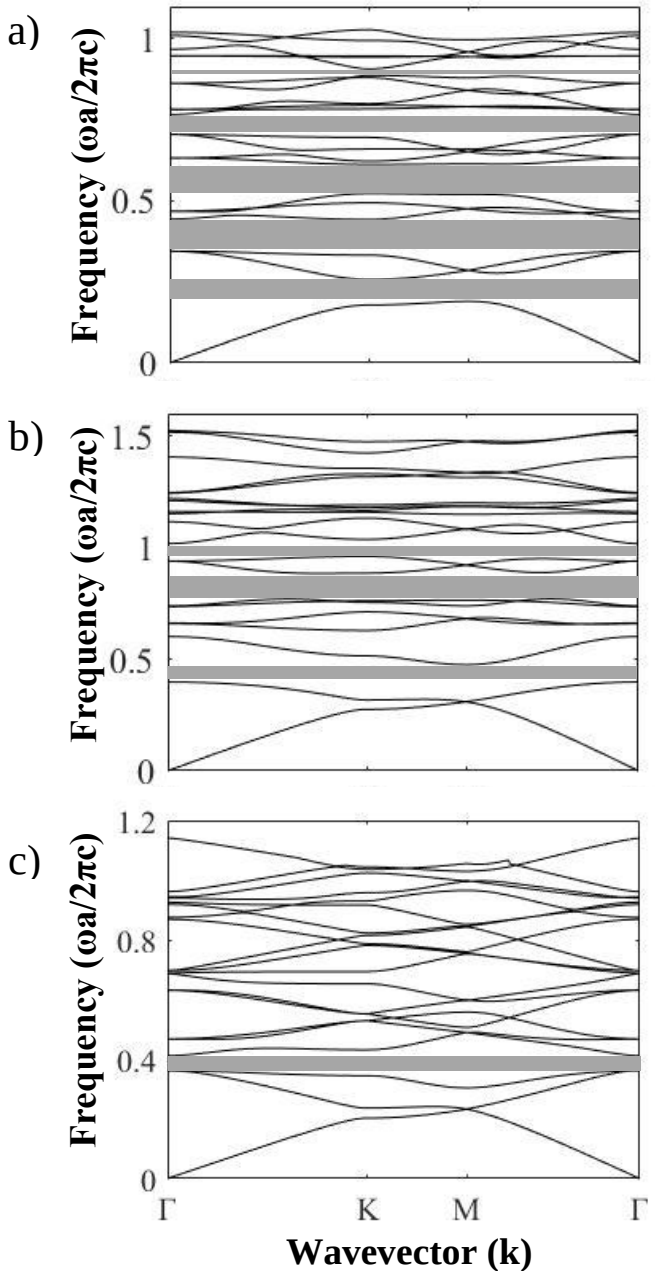

Figure 5. TM band structures for $(3 \cdot 6)^2$ ATs. (a) Direct structure ($\varepsilon_{hexagon}$ = 16, $\varepsilon_{triangle}$ = 2, R = 0.7). The maximum bandgap sizes are 14.4% (1-2 gap), 24.8% (3-4 gap), and 15.8% (6-7 gap) gap-to-midgap ratio. (b) Direct structure ($\varepsilon_{hexagon}$ = 2, $\varepsilon_{triangle}$ = 16, R = 0.7). The maximum bandgap size is 17.8% (2-3 gap) gap-to-midgap ratio. (c) Inverse structure (ε_{matrix} = 16, R = 0.8). The maximum bandgap size is 13.3% (3-4 gap) gap-to-midgap ratio. Bandgaps with sizes less than 5% are not discussed here or in the text.

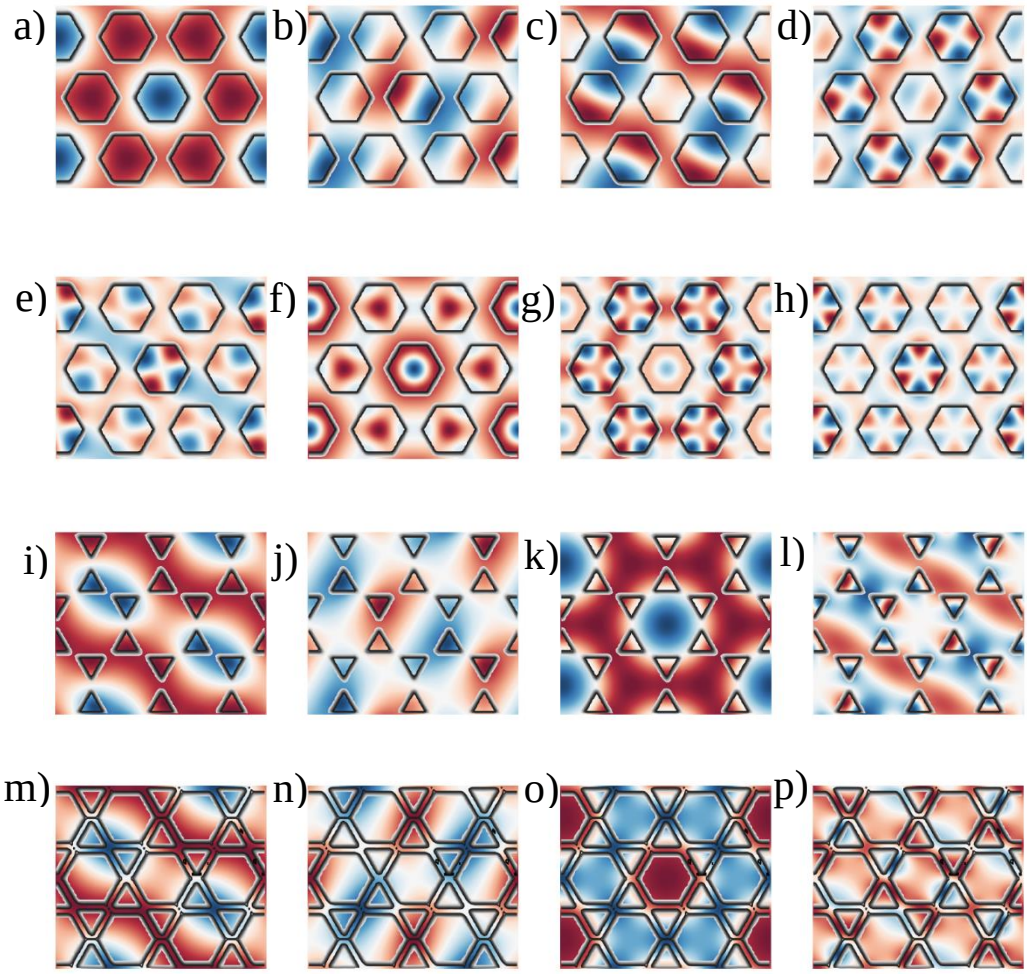

Figure 6. TM electric displacement field density for the $(3 \cdot 6)^2$ ATs. (a)-(h) Direct structure, bands 1-8 ($\varepsilon_{hexagon}$= 16, $\varepsilon_{triangle}$ = 2, R = 0.8). The bandgaps are found between bands 1 and 2, 3 and 4, and 6 and 7. (i)-(l) Direct structure, bands 1-4 ($\varepsilon_{hexagon}$ = 2, $\varepsilon_{triangle}$ = 16, R = 0.8). The bandgap is found between bands 2 and 3. (m)-(p) Inverse structure, bands 1-4 (ε_{matrix} = 12, R = 0.8). The bandgap is found between bands 3 and 4.

The sequences of strong field concentration in the hexagonal cross-section rods (i.e., in phase oscillations) and one or more nodes in the same (i.e., antiphase oscillations) are consistent with Lorenz-Mie scattering.[52] The bandgaps form due to the energy differences between consecutive Lorenz-Mie resonances in the high dielectric rods. Similarly, the mode field distributions for the structure with high dielectric triangular rods [Figures 6(i)-(l)] show characteristic features of Lorenz-Mie bandgap origin, i.e., energy difference between in-phase [Figures 6(i)-(j)] and anti-phase [Figures 6(k)-(l)] oscillations (2-3 bandgap). Unlike the direct $(3 \cdot 6)^2$ AT, the field distributions for the inverse structure [Figures 6(m)-(p)] suggests that the 3-4 TM gap origin stems from the re-distribution of the mode from the low (i.e., hexagons) to the high dielectric constant material (i.e., matrix).

The TE band diagrams for the direct and inverse $(3 \cdot 6)^2$ ATs are provided in the Supplementary Information (Figure S3). We expected that the inverse structures would have large TE bandgaps because of the interconnected matrix regions. To achieve large gap sizes, the veins of high dielectric should be unbroken so that continuous TE field lines can be contained within them. As expected, the inverse structure promotes large 1-2 and 3-4 bandgaps with sizes up to 28.2% and 30.6% gap-to-midgap ratio (ε_{matrix} = 16, R = 0.7). Conversely, relatively small TE bandgap sizes are observed in the direct structures of isolated dielectric rods, up to 14.4% gap-to-midgap ratio (ε_{matrix} = 16, R = 0.7).

The refraction properties of the direct $(3 \cdot 6)^2$ ATs were determined using equifrequency contour EFC analysis and FDTD simulations. The TM second band was chosen for these studies because it is highly anisotropic (i.e., 25% and 22% frequency change across the irreducible Brillouin zone for high dielectric hexagons and triangles, respectively). Moreover, Band 2 exhibits low degeneracy with surrounding bands and so is likely to show one refraction solution for each EFC analysis and simulation. The contours of equal frequencies for the structure having high dielectric hexagonal rods are mapped over the first Brillouin zone with high symmetry points labeled in Figure 7(a). The EFC analysis is performed for a Gaussian beam with a normalized frequency of 0.28 and incident angle ($\boldsymbol{k_{incident}}$) of 45° on the ΓK surface. Negative refraction is predicted because the incident angle and the group velocity of the refracted beam ($\boldsymbol{v_{g,refraction}}$) lie on the same side of the normal. The left-handedness of the refraction is confirmed from the obtuse angle between the group velocity $\boldsymbol{v_{g,PC}}$ and phase velocity $\boldsymbol{v_{\phi,PC}}$ in the simulated evolution of the electromagnetic field [Figure 7(b)]. The concave contour lines around the Γ high symmetry point of the EFC, indicate a wide availability of incident angles with negative refraction. Consequently, we establish the frequency range for nearly AANR from the analysis of EFCs [Figure 7(c)]. The region corresponding to negative refraction is limited for low frequency and incident angle because of small regions of convex curvature.

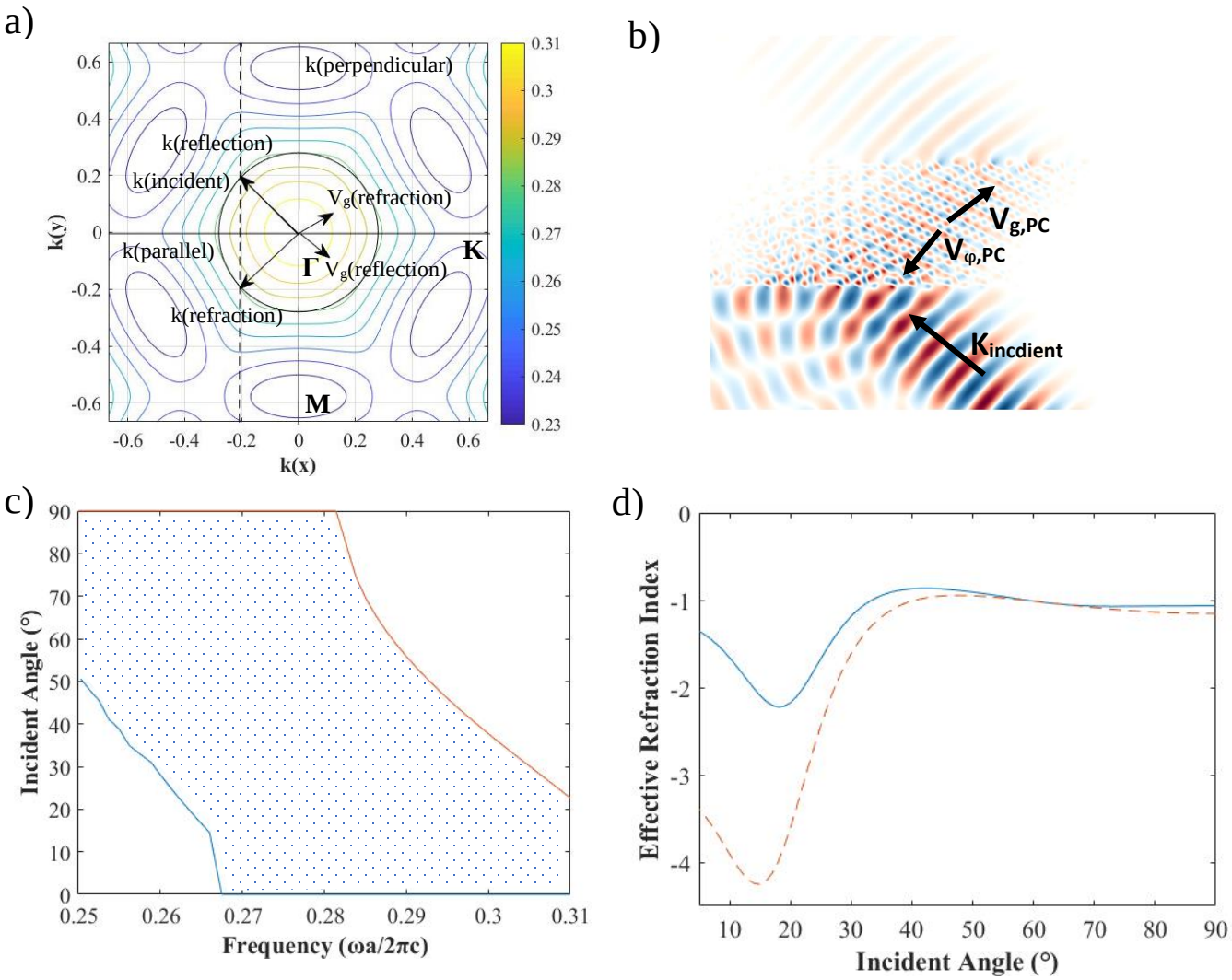

Figure 7. Negative refraction properties for TM band 2 in the direct $(3 \cdot 6)^2$ AT ($\varepsilon_{hexagon}$ = 16, $\varepsilon_{triangle}$ = 2, R = 0.8). (a) EFC analysis predicting LHNR for a frequency of $\omega a/2\pi c$ = 0.28 and an angle of incidence of 45° on the ΓK interface. The group velocity vectors show direction and not magnitude. (b) FDTD simulation using a Gaussian beam with frequency and incident angle from (a) confirming LHNR. Blue, white, and red correspond, respectively, to negative, zero, and positive E_z field. (c) The effect of frequency on the angular range of negative refraction. (d) The effect of incident angle on the effective refractive index for frequencies in the AANR range. The solid and dashed lines represent frequency $\omega a/2\pi c$ = 0.28 and $\omega a/2\pi c$ = 0.27, respectively.

For high frequency and incident angle, negative refraction is blocked by the bandgap. Key conditions for imaging with ultrahigh resolution include AANR and effective refractive index of negative one. The AANR property is obtained for normalized frequency values between 0.27 and 0.28. For this frequency region, the effect of the incident angle on the n_{eff} was calculated using Snell's Law [Figure 7(d)]. The curves level off around $n_{eff} = -1$. In particular, the values of n_{eff} is close to negative one for an incident angle of 35° and normalized frequency of 0.28.

The refraction properties are presented in Figure 8 for the second TM band with high dielectric triangular rods. Figure 8(a) shows the EFC analysis for a Gaussian beam with a normalized frequency of 0.32 and incident angle of 45°. We predict LHNR properties from the EFC analysis, and simulations are in agreement with this finding [Figure 8(b)]. For normalized frequencies between 0.32 and 0.34, n_{eff} is near negative one for incident angles greater than ~50° [Figure 8(c, d)]. The refraction properties of the second TM band for the inverse structure are shown in Figure 9. The EFC analysis and simulated propagation of the electromagnetic field verify LHNR for the normalized frequency 0.34 and incidence angle of 45° [Figure 9(a-b)]. The inverse structure promotes AANR for normalized frequency between ~0.32 and 0.34, and n_{eff} maintains a value near negative one for incident angles larger than 45° [Figure 9(c-d)].

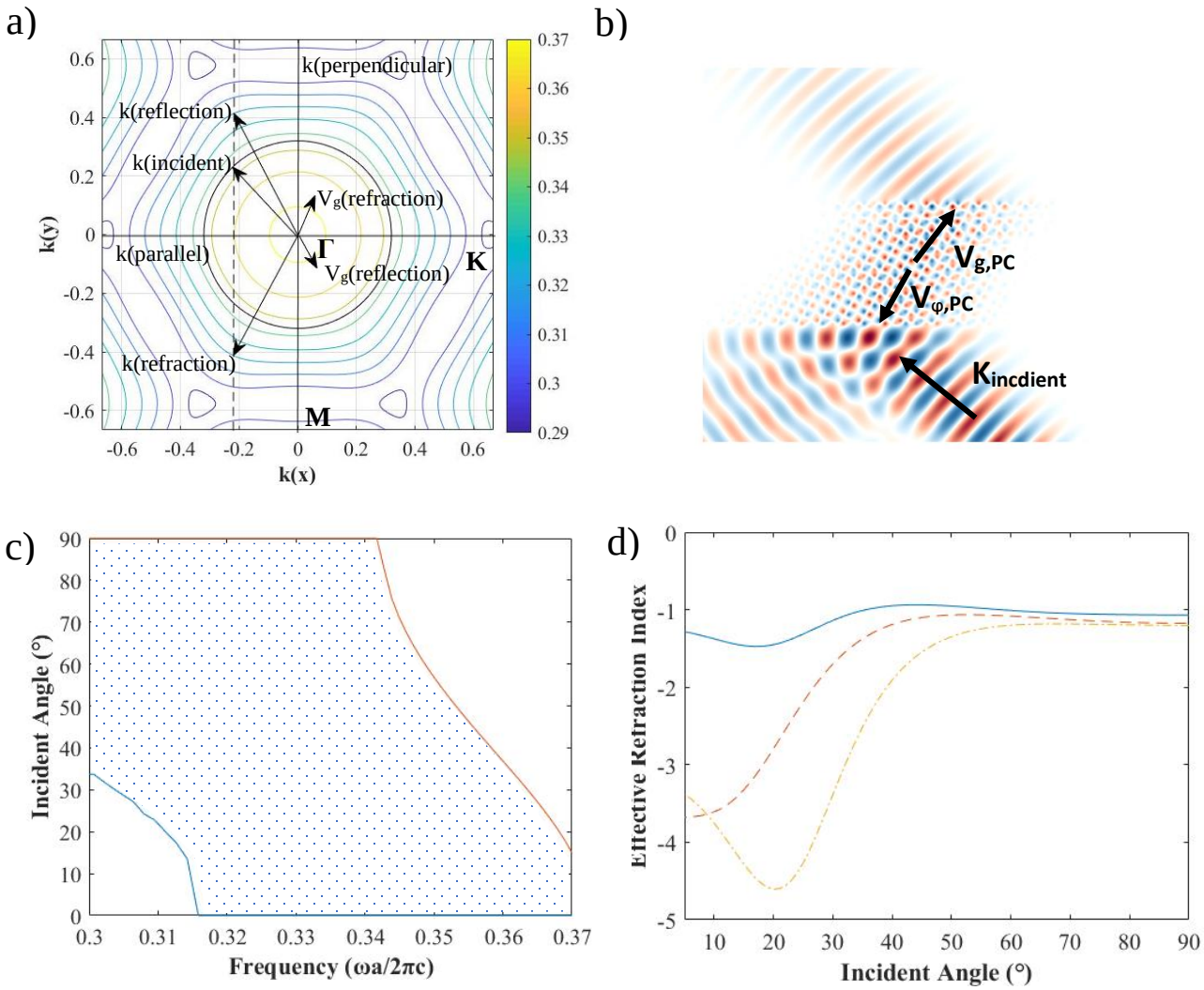

Figure 8. Negative refraction properties for TM band 2 in the direct $(3 \cdot 6)^2$ AT ($\varepsilon_{hexagon}$ = 2, $\varepsilon_{triangle}$ = 16, R = 0.8). (a) EFC analysis predicting LHNR for a frequency of $\omega a/2\pi c$ = 0.32 and an angle of incidence of 45° on the ΓK interface. The group velocity vectors show direction and not magnitude. (b) FDTD simulation using a Gaussian beam with frequency and incident angle from (a) confirming LHNR. Blue, white, and red correspond, respectively, to negative, zero, and positive E_z field. (c) The effect of frequency on the angular range of negative refraction. (d) The effect of incident angle on the effective refractive index for frequencies in the AANR range. The solid, dashed, and dash-dot lines represent frequency $\omega a/2\pi c$ = 0.34, $\omega a/2\pi c$ = 0.33, and $\omega a/2\pi c$ = 0.32, respectively.

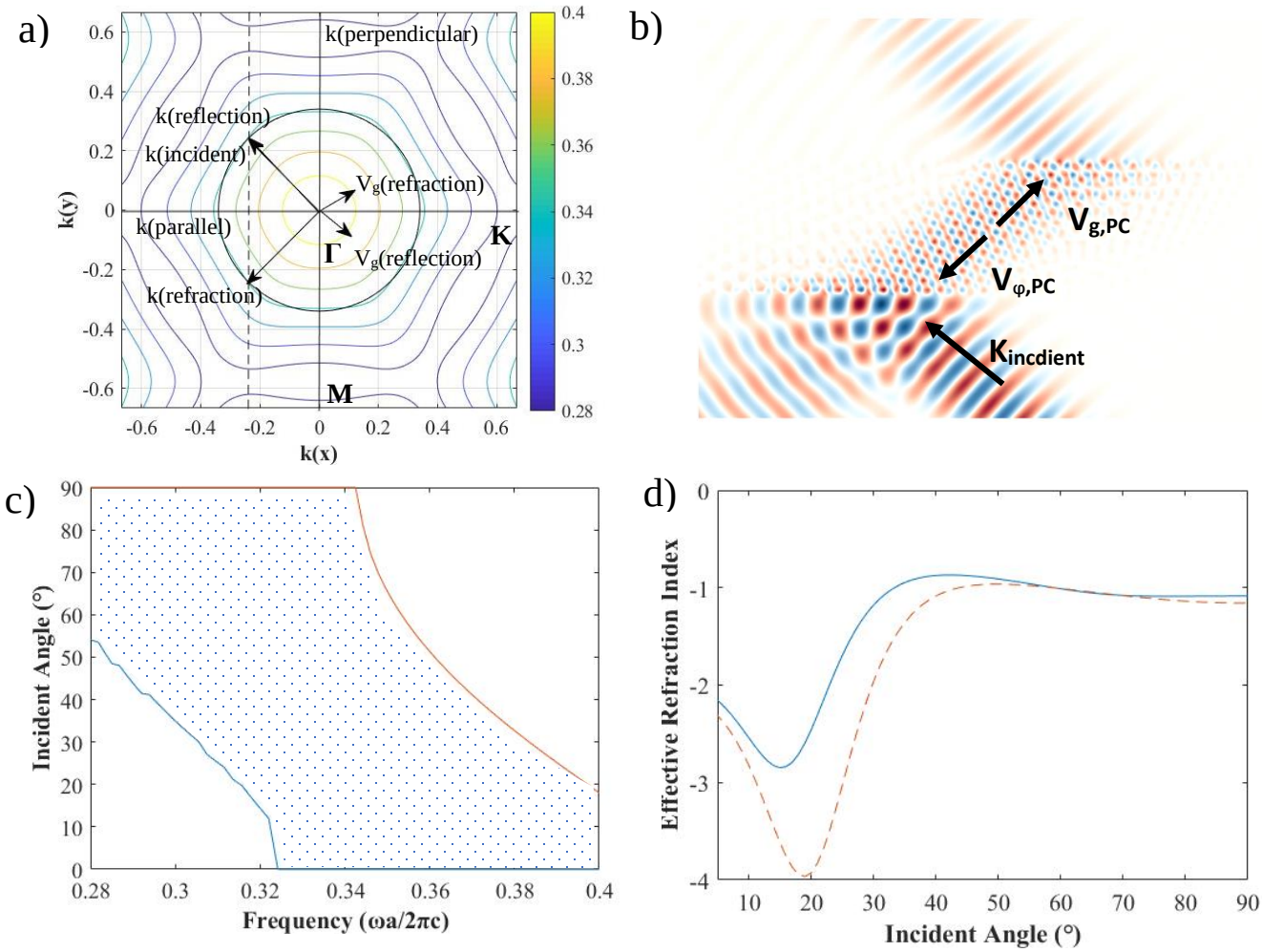

Figure 9. Negative refraction properties for TM band 2 in the inverse $(3 \cdot 6)^2$ AT (ε_{matrix} = 12, R = 0.8). (a) EFC analysis predicting LHNR for a frequency of $\omega a/2\pi c$ = 0.34 and an angle of incidence of 45° on the ΓK interface. The group velocity vectors show direction and not magnitude. (b) FDTD simulation using a Gaussian beam with frequency and incident angle from (a) confirming LHNR. Blue, white, and red correspond, respectively, to negative, zero, and positive E_z field. (c) The effect of frequency on the angular range of negative refraction. (d) The effect of incident angle on the effective refractive index for frequencies in the AANR range. The solid and dashed lines represent frequency $\omega a/2\pi c$ = 0.34 and $\omega a/2\pi c$ = 0.33, respectively.

The refraction properties for the TE band 2 were also analyzed from the EFC for the inverse structure as shown in the Supplemental Information (Figure S4). LHNR for the normalized frequency of 0.34 and incident angle of 30° is determined, but AANR was not present for this structure.

The effect of the basis size parameter R on the normalized frequency range for AANR in TM band 2 is shown in Figure 10. The frequency region for AANR expands as R increases toward the condition for tangent dielectric rods in the direct structures [Figure 10(a-b)]. Interestingly, this is the opposite trend with respect to PhC bandgap size. The latter trend likely occurs because increasing the filling fraction compresses the bands to lower frequency and in the extreme case closes the gaps. Figure 10(c) presents the AANR region for the inverse structure, which shows the expected dependence on basis size parameter (i.e., compressing bands reduces band anisotropy, and limits AANR).

To demonstrate point source imaging, a continuous point source with normalized frequency of 0.34 is placed one unit cell away from the PhC flat lens ($\varepsilon_{\text{hexagon}} = 16$, $\varepsilon_{\text{triangle}} = 2$, R = 0.8). Figure 11(a) illustrates the point source simulations, in which the image is obtained for a PhC with thickness of 2 unit cells. Subwavelength imaging is demonstrated and a half-wave distance of 0.42λ was measured parallel to the PhC surface.

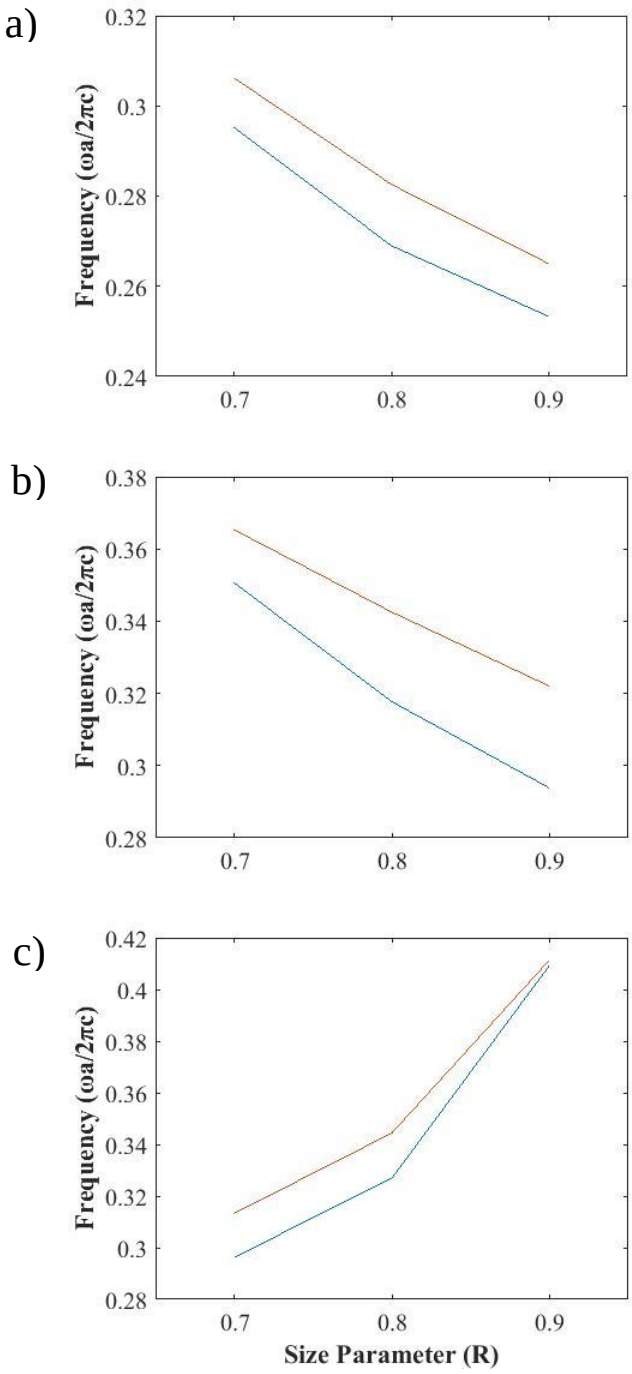

Figure 10. The effect of R on the frequency range of AANR in the $(3 \cdot 6)^2$ AT. (a) direct structure ($\varepsilon_{hexagon}$ = 16, $\varepsilon_{triangle}$ = 2, R = 0.8) (b) direct structure ($\varepsilon_{hexagon}$ = 2, $\varepsilon_{triangle}$ = 16, R = 0.8) (c) inverse structure (ε_{matrix} = 12, R = 0.8).

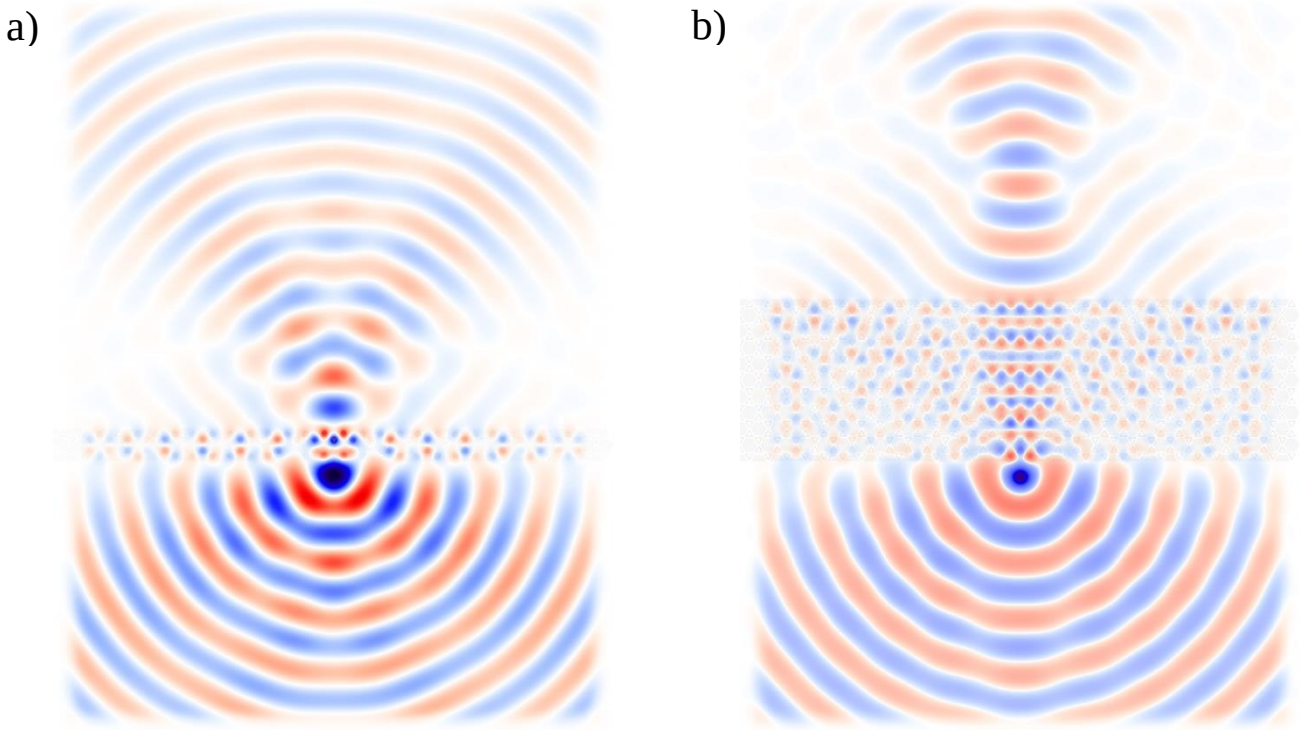

Figure 11. Point source simulations for the direct $(3 \cdot 6)^2$ AT using FDTD method. (a) Continuous point source with frequency $\omega a/2\pi c = 0.34$ irradiates a PhC flat lens having 2 unit cells of the structure ($\varepsilon_{hexagon} = 16$, $\varepsilon_{triangle} = 2$, R = 0.8), demonstrating imaging (b) Continuous point source with frequency $\omega a/2\pi c = 0.34$ irradiates a PhC flat lens having 10 unit cells of the structure, demonstrating self-collimation.

The artifacts in the image are due to absorption of light by the perfectly matched layer, and weak refraction for high and low angles of incidence, respectively. When the light propagates through the thick PhC (i.e., 10 unit cells) self-collimation is observed for the incident angle in the range of (-25°, 25°)[Figure 11(b)]. Self-collimation exhibits diffraction-free light propagation without the need for guiding boundaries and has been used in applications, including waveguiding, beam steering, switching, and sensing, to name a few.[22]

Conclusion

In summary, we find large TM bandgaps for the $(3 \cdot 6)^2$ semi-regular tiling, consistent with the self-assembly of shape-binary mixtures. These large bandgaps are comparable in size to those of high precision lithographic structures, but can be fabricated by colloidal assembly. In addition, the bandgaps open at low dielectric contrasts so that the structures can be made from common materials. The physical origin of the bandgaps in the direct structures is found to be Lorenz-Mie resonances in anisotropic scatterers, while in the inverse structures it is attributed to air band-dielectric band transitions. All-angle negative refraction is predicted based on contours of equal frequency and finite difference time domain (FDTD) simulations. The frequency range of AANR can be tuned to the desired frequency region using the rod

spacing. Moreover, the effective refractive index is predicted to be close to -1 for certain frequencies inside the AANR range, which enables to superlensing and self-collimation. For hexagonal and triangular building blocks with dielectric constants of 16 and 2, respectively, the half-wave distance for the TM polarized source is determined to be 0.42 λ, confirming subwavelength imaging. Recently, thermodynamic simulations of shape-binary mixtures with enthalpic shape-specific or edge-specific patches predict the self-organization of all 11 semi-regular tilings. The computational study reported here opens a frontier for research to manipulate multiple anisotropic shape effects for photonics.

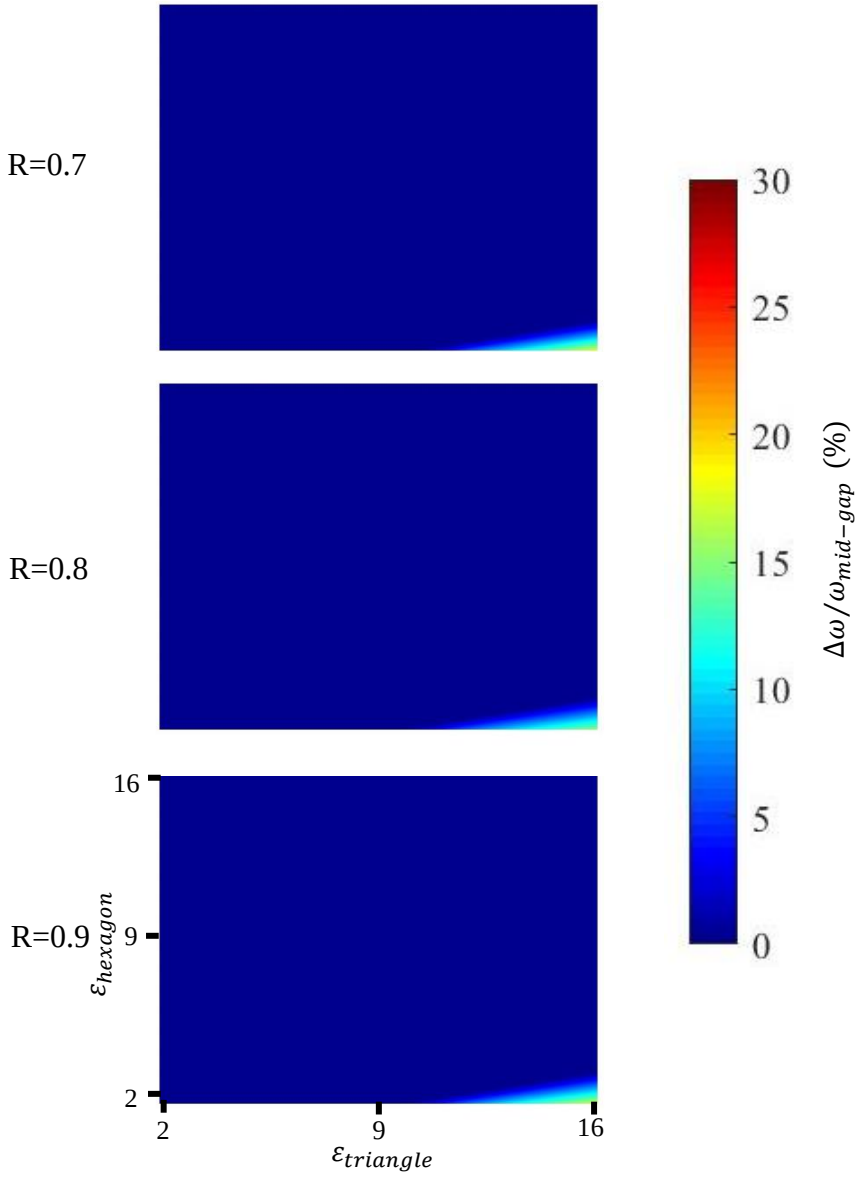

Figure S1. Contour maps of the 2-3 TM bandgap size (gap-to-midgap ratio) in the direct $(3 \cdot 6)^2$ structure as a function of dielectric contrasts and basis spacing parameter.

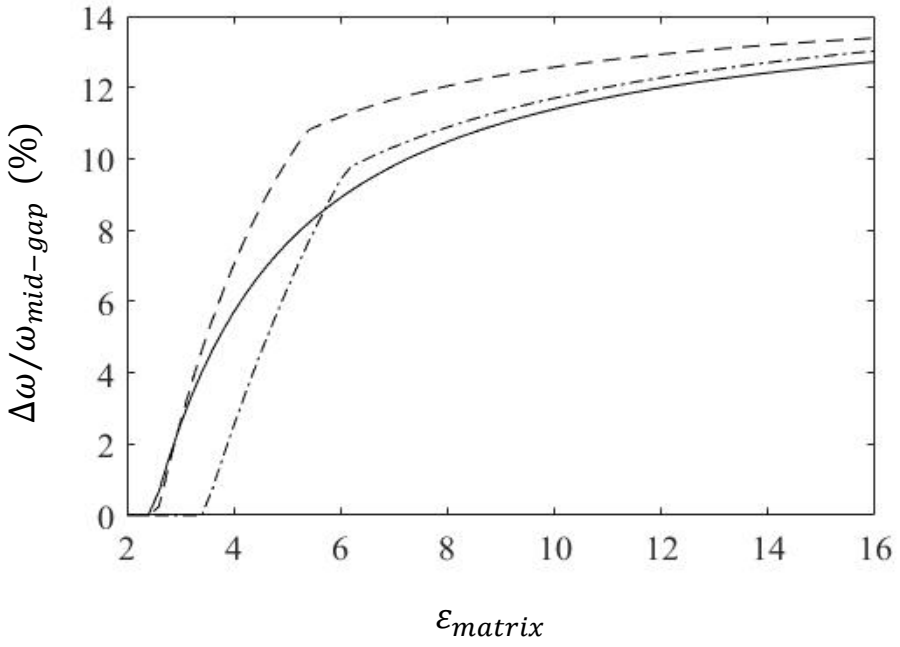

Figure S2. The effect of the dielectric constant of the matrix on the size of the 3-4 bandgap in the $(3 \cdot 6)^2$ inverse structure. The solid, dashed and dash-dot lines represent R=0.7, R = 0.8 and R=0.9,

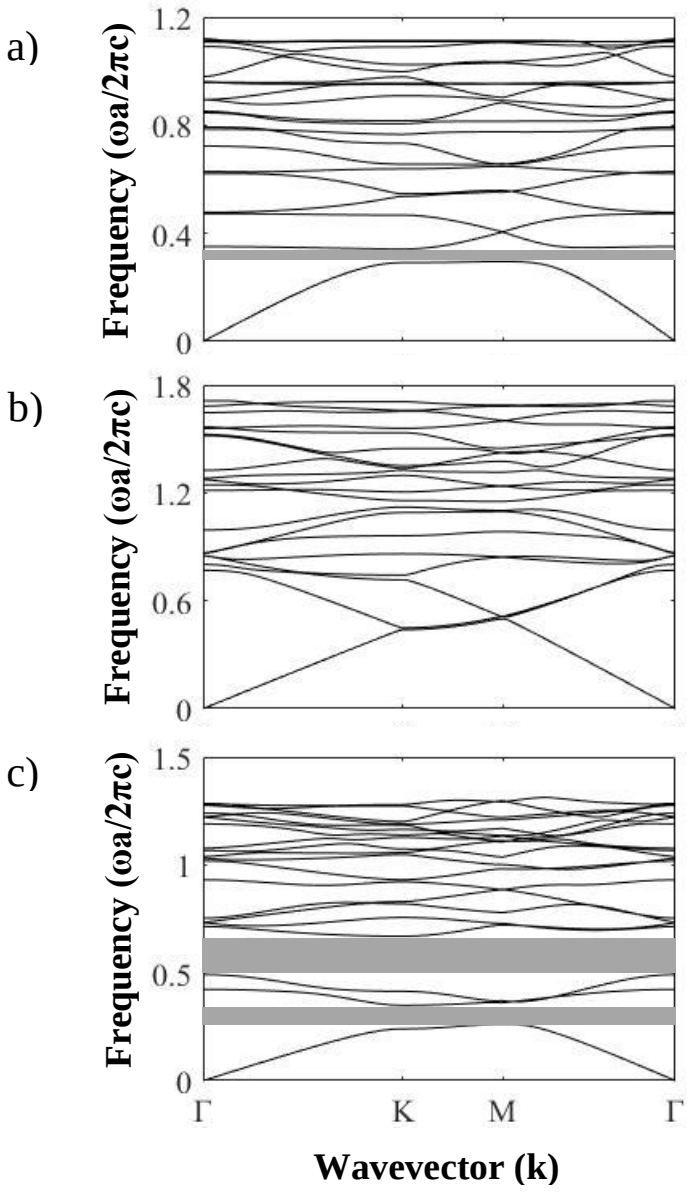

Figure S3. TE band structures for $(3 \cdot 6)^2$ ATs. (a) Direct structure ($\varepsilon_{hexagon}$ = 16, $\varepsilon_{triangle}$ = 2, R = 0.7). The maximum bandgap size is 14.4% (1-2 gap) gap-to-midgap ratio. (b) Direct structure ($\varepsilon_{hexagon}$ = 2, $\varepsilon_{triangle}$ = 16, R = 0.7). No sizable bandgaps are found. (c) Inverse structure (ε_{matrix} = 16, R = 0.8). The maximum bandgap sizes are 28.2% (1-2 gap), and 30.6% (3-4 gap) gap-to-midgap ratio. Bandgaps with sizes less than 5% are not discussed here or in the text.

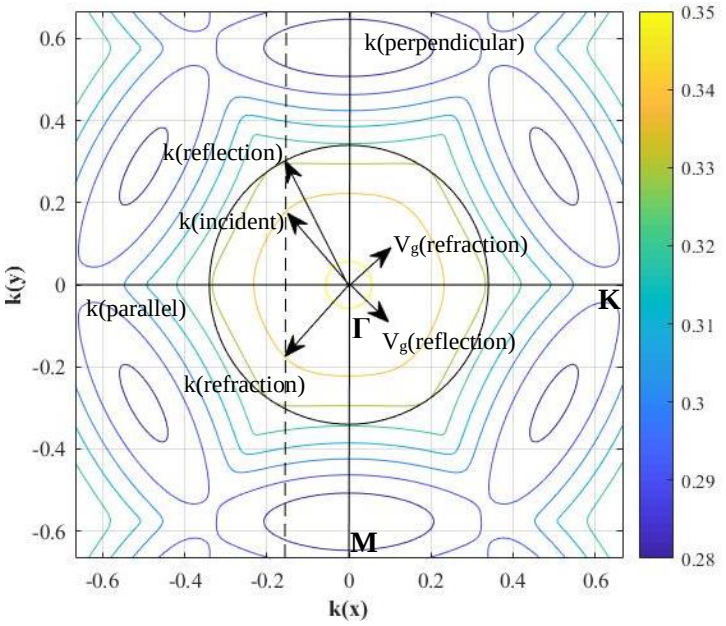

Figure S4. Negative refraction properties for TE band 2 in the inverse $(3 \cdot 6)^2$ AT ($\varepsilon_{matrix} = 16$, R = 0.7). (a) EFC analysis predicting LHNR for a frequency of $\omega a/2\pi c = 0.34$ and an angle of incidence of 30° on the ΓK interface. The group velocity vectors show direction and not magnitude

References

1. Joannopoulos, J. D.; Villeneuve, P. R.; Fan, S. Photonic crystals: putting a new twist on light. *Nature* **1997**, *386*, 143-149.
2. Yan, H.; Gu, C.; Yang, C.; Liu, J.; Jin, G.; Zhang, J.; Hou, L.; Yao, Y. Hollow core photonic crystal fiber surface-enhanced Raman probe. *Appl. Phys. Lett.* **2006**, *89*, 204101.
3. Yang, J.; Heo, J.; Zhu, T.; Xu, J.; Topolancik, J.; Vollmer, F.; Ilic, R.; Bhattacharya, P. Enhanced photoluminescence from embedded PbSe colloidal quantum dots in silicon-based random photonic crystal microcavities. *Appl. Phys. Lett.* **2008**, *92*, 261110.
4. Baba, T. Slow light in photonic crystals. *Nat. Photonics* **2008**, 2, 465-473.
5. Jovanović, D.; Gajić, R.; Hingerl, K. Refraction and band isotropy in 2D square-like archimedean photonic crystal lattices. *Opt. Express* **2008**, *16*, 4048-4058.
6. Johnson, S.G.; Fan, S.; Villeneuve, P. R.; Joannopoulos, J. D.; Kolodziejski, L. Guided modes in photonic crystal slabs. *Phys. Rev. B* **1990**, *60*, 5751-5758.
7. Boroditsky, M.; Krauss, T. F.; Coccioli, R.; Vrijen, R.; Bhat, R.; Yablonovitch, E. Light extraction from optically pumped light-emitting diode by thin-slab photonic crystals. *Appl. Phys. Lett.* **1999**, *75*, 1036-1038.
8. Centeno, E.; Ciraci, C.; Felbacq, D.; Cassagne, D. Second harmonic localization in nonlinear photonic crystals. *Proc. SPIE* **2008**, *6989*, 698915.

9. Meisels, R.; Gajic, R.; Kuchar, F.; Hingerl, K. Negative refraction and flat-lens focusing in a 2D square-lattice photonic crystal at microwave and millimeter wave frequencies. *Opt. Express* **2006**, *14*, 6766-6777.
10. Man, W.; Florescu, M.; Matsuyama, K.; Yadak, P.; Nahal, G.; Hashemizad, S.; Williamson, E.; Steinhardt, P.; Torquato, S.; Chaikin, P. Photonic band gap in isotropic hyperuniform disordered solids with low dielectric contrast. *Opt. Express* **2013**, *21*, 19975.
11. Edagawa, K.; Kanoko, S.; Notomi, M. Photonic amorphous diamond structure with a 3D photonic band gap. *Phys. Rev. Lett.* **2008**, *100*, 013901.
12. Edagawa, K. Photonic crystals, amorphous materials, and quasicrystals. *Sci. Technol. Adv. Mater.* **2014**, 15, 34805.
13. Jovanović, D.; Gajić, R.; Hingerl, K. Refraction and band isotropy in 2D square-like archimedean photonic crystal lattices. *Opt. Express* **2008**, *16*, 4048-4058.
14. David, A.; Fujii, T.; Matioli, E.; Sharma, R.; Nakamura, S.; Denbaars, S. P.; Weisbuch, C.; Benisty, H. GaN light-emitting diodes with Archimedean lattice photonic crystals. *Appl. Phys. Lett.* **2006**, *88*, 073510.
15. Stelson, A. C.; Britton, W. A.; Liddell Watson, C. M. Photonic crystal properties of self-assembled Archimedean Tilings. *J. Appl. Phys*. **2017**, *121*, 023101.
16. Man, W.; Florescu, M.; Williamson, E. P.; He, Y.; Hashemizad, S. R.; Leung, B. Y. C.; Liner, D. R.; Torquato, S.;. Chaikin, P. M; Steinhardt, P. J. Isotropic band gaps and

freeform waveguides observed in hyperuniform disordered photonic solids. *Proc. Natl. Acad. Sci. U. S. A.* **2013**, *110*, 15886.

17. Tsitrin, S.; He, Y.; Hewatt, S.; Leung, B.; Man, W.; Florescu, M.; Steinhardt, P. J.; Torquato, J. S.; Chaikin, P. Cavity modes study in hyperuniform disordered photonic bandgap materials frontiers. *Proceedings Optics 2012/Laser Science XXVIII,* Optical Society of America, **2012**, FTh3F.4.
18. David, A.; Fujii, T.; Matioli, E.; Sharma, R.; Nakamura, S.; DenBaars, S. P.; Weisbuch, C.; Benisty, H. GaN light-emitting diodes with Archimedean lattice photonic crystals. Appl. Phys. Lett. **2006**, *88*, 073510.
19. Johnson, S. G.; Joannopoulos, J. D. Block-iterative frequency-domain methods for Maxwell's equations in a planewave basis. *Opt. Express*, **2001**, *8*, 173.
20. Joannopoulos, J. D; Johnson, S. G.; Winn, J. N.; Meade, R. D. Photonic Crystals Molding the Flow of Light, 2nd ed.; Princeton University Press: Princeton, New Jersey, 2008.
21. Gajić, R.; Meisels, R.; Kuchar, F.; Hingerl, K. All-angle left-handed negative refraction in Kagomé and honeycomb lattice photonic crystals. *Phys. Rev. B* **2006**, *73*, 165310.
22. Kosaka, H.; Kawashima, T.; Tomita, A.; Notomi, M.; Tamamura, T.; Sato, T.; Kawakami S. Self-collimating phenomena in photonic crystals. *Appl. Phys. Lett.* **1999**, *74*, 1212.

23. Baba, T. Slow light in photonic crystals. *Nat. Photonics* **2008**, 2, 465-473.

24. Krauss, T. F. Slow light in photonic crystal waveguides. *J. Phys. D: Appl. Phys.* **2007**, *40*, 2666-2670.

25. Maldovan, M; Thomas, E. L. Periodic materials and interference lithography. Wiley-VCH: Weinheim, 2009.

26. Fischer, J.; von Freymann, G.; Wegener, M. The materials challenge in diffraction-unlimited direct-laser-writing optical lithography. *Adv. Mater.* **2010**, *22*, 3578-3582.

27. Galisteo-López, J. F.; Ibisate, M.; Sapienza, R.; Froufe-pérez, L. S.; Blanco, A.; Lopez, C. Self-assembled photonic structures. *Adv. Mater.* **2011**, *23*, 30-69.

28. Busch, K.; John, S. Photonic band gap formation in certain self-organizing systems. *Phys. Rev. E* **1998**, *58*, 3896-3908.

29. Li, Z.; Wang, J.; Gu, B., Full band gap in FCC and BCC photonic band gap structure: Nonspherical atom. *J. Phys. Soc. Jpn.* **1998**, *67*, 3288-3291.

30. Li, Z.-Y.; Zhang, Z.-Q., Photonic bandgaps in disordered inverse-opal photonic crystals. *Adv. Mater.* **2001**, *13*, 433-436.

31. Ho, K. M.; Chan, C. T.; Soukoulis; C. M. Existence of a photonic gap in periodic dielectric structures. *Phys. Rev. Lett.* **1990**, *65*, 3152-3155.

32. Xia, Y.; Gates, B.; Li, Z.-Y. Self-Assembly approaches to three-dimensional photonic crystals. *Adv. Mater.* **2001**, *13*, 409-413.

33. Garcia-Santamaria, F.; Miyazaki, H. T.; Urquia, A.; Ibisate, M.; Belmonte, M.; Shinya, N.; Messeguer, F.; Lopez, C. Nanorobotic manipulation of microspheres for on-chip diamond architectures. *Adv. Mater.* **2002**, *14*, 1144-1147.

34. Ducrot, E.; He, M.; Yi, G.-R.; Pine, D. J. Colloidal alloys with pre-assembled clusters and spheres. *Nat. Mater.* **2017**, *16*, 652–657.

35. Dommelen, R. Van; Fanzio, P.; Sasso, L. Surface Self-Assembly of Colloidal Crystals for Micro- and Nano-Patterning. *Adv. Colloid Interface Sci.* 2018, 251, 97-114.

36. Sugimoto, T.; Khan, M. M.; Muramatsu, A. Preparation of monodisperse peanut-type alpha-Fe2O3 particles from condensed ferric hydroxide gel. *Colloids Surf. A.* **1993**, *70*, 167-169.

37. Lee, S. H.; Liddell, C. M. Anisotropic magnetic colloids: A strategy to form complex structures using nonspherical building blocks. *Small* **2009**, *5*, 1957-1962.

38. Mock, E. B.; De Bruyn, H.; Hawkett, B. S.; Gilbert, R. G.; Zukoski, C. F. Synthesis of anisotropic nanoparticles by seeded emulsion polymerization. *Langmuir* **2006**, *22*, 4037-4043.

39. Kim, J.; Larsen, R.J.; Weitz, D.A. Synthesis of Nonspherical Colloidal Particles with Anisotropic Properties. *Journal of the American Chemical Society* **2006**, *128*, 12274-14377.

40. Fung, E. Y.; Muangnapoh, K.; Liddell Watson, C. M. Anisotropic PC building blocks: colloids tuned from mushroom-caps to dimers. *Journal of Materials Chemistry*, **2012**, *22*, 10507-10513.

41. Jeong, J.; Kim, W.; Park, S.; Yoon, T.; Chung, B. H. Synthesis and characterization of various-shaped C60 microcrystals using alcohols as antisolvents. Journal of Physical Chemistry C 2010, 114, 12976-12981.

42. Park, C.; Yoon, E.; Kawano, M.; Joo, Taiha; Choi, H.-C. Self-crystallization of C70 cubes and remarkable enhancement of photoluminescence. Angewandte Chemie International Edition 2010, 49, 9670-9675.

43. Penterman, S.; Liddell Watson, C. M. Anisometric C_{60} fullerene colloids assisted by structure-directing agent. *Crystal Engineering Communications* **2016**, *18*, 1775-1781.

44. Badaire, S.; Cotton-Bizonne, C.; Woody, J. W.; Yang, A.; Stroock, A. D. Shape selectivity in the assembly of lithographically designed colloidal particles. *Journal of the American Chemical Society* **2007**, *129*, 40-41.

45. Panda, P.; Yuet, K. P.; Hatton, T. A.; Doyle, P. S. Tuning curvature in flow lithography: a new class of concave/convex particles. *Langmuir* **2009**, *25*, 5986-5992.

46. Rolland, J. P.; Maynor, B. W.; Euliss, L. E.; Exner, A. E.; Denison, G. M.; DeSimone, J. M. Direct fabrication and harvesting of monodisperse, shape-specific nanobiomaterials. *Journal of the American Chemical Society* **2005**, *127*, 10096-10100.

47. Millan, J. A.; Ortiz, D.; van Anders, G.; Glotzer, S. C. Self-assembly of Archimedean tilings with enthalpically and entropically patchy polygons. *ACS Nano* **2014**, *8*, 2918.

48. Gajic, R.; Meisels, R.; Kuchar, F.; Hingerl, K. Refraction and rightness in photonic crystals. *Opt. Express* **2005**, *13*, 8596-8605.

49. Vermolen, E. C. M.; Thijssen, J. H. J.; Moroz, A.; Megens, M.; van Blaaderen, A. Comparing photonic band structure calculation methods for diamond and pyrochlore crystals. *Opt. Express* **2009**, *17*, 6952.

50. Chan, C. T.; Datta, S.; Ho, K. M.; Soukoulis, C. M. A7 structure: a family of photonic crystal. *Phys. Rev. B* **1994**, *50*, 1988-1991.

51. Gao, J.-W.; Zhang, Y.; Ba, N.; Cui, C.-L.; Wu, J.-H. Dynamically induced double photonic bandgaps in the presence of spontaneously generated coherence. *Opt. Lett.* **2010**, *35*, 709-711.

52. Scharrer, M.; Yamilov, A.; Wu, X.; Cao, H.; Chang, R. P. H. Ultraviolet lasing in high-order bands of three-dimensional ZnO photonic crystals. *Applied Physics Letters* **2006**, *88*, 201103-1.